Hybrid exchange density functional study of vicinal anatase TiO$_2$ surfaces

F. F. Sanches,[1,*] G. Mallia,[1] L. Liborio,[1] U. Diebold,[2] and N. M. Harrison[1,3]

[1]*Thomas Young Centre, Department of Chemistry, Imperial College London, South Kensington, London SW7 2AZ, United Kingdom*
[2]*Institute of Applied Physics, Vienna University of Technology, Wiedner Hauptstrasse 8-10/134, A-1040 Vienna, Austria*
[3]*STFC, Daresbury Laboratory, Daresbury, Warrington WA4 4AD, United Kingdom*

The observation of photocatalytic water splitting on the surface of anatase TiO$_2$ crystals has stimulated many investigations of the underlying processes. Nevertheless, a molecular-level understanding of the reaction is not available. This requires knowledge of the crystal facets present, the atomistic structure of the surfaces, and thus the reaction sites involved. In this paper we establish the atomistic structure of two surfaces, vicinal to the low-energy (101) surface. We compute the relative stability and electronic properties of the (514) and (516) surfaces and compare these to the low-index (101), (001), and (100) surfaces. The (516) surface is remarkably stable, and is predicted to contribute significantly to the surface area of a crystallite in equilibrium. We simulate constant current scanning tunneling microscopy images and, by comparing with those measured, we conclude that a surface previously observed in a miscut single crystal is the (516) surface described here. The computed stability of this surface indicates that it will be present in TiO$_2$ nanostructures and the relative positions of its band edges suggests that it will play a significant role in the water-TiO$_2$ reactions in solar water splitting.

PACS number(s): 73.20.−r, 31.15.A−, 68.35.bg

I. INTRODUCTION

Current concerns over global warming have led to numerous international and regional agreements/treaties pledging to reduce the amount of anthropogenic CO$_2$ being emitted. The European Union, for example, has committed to reducing its CO$_2$ emissions by 20% from 1990 levels [1]. Increased use of renewable energy sources will play a key role in meeting these targets [1]. One attractive option is solar water splitting. This would harness an abundant renewable energy source and provide means of storing solar energy in the form of hydrogen gas and as derivatives thereof. Since Fujishima *et al.* first demonstrated photolytic splitting of water on TiO$_2$ under UV irradiation [2], TiO$_2$ has been extensively studied as a photocatalyst in various photochemical processes (including solar water splitting) [3–7].

In photoelectrochemical water-splitting systems the photoanode doubles as a light absorber and water oxidation catalyst [3]. In order to increase the surface area and, thus, maximize the number of photogenerated holes that reach the surface, nanostructured TiO$_2$ films are commonly used [3–6]. Typically, the films are prepared from a colloidal paste of anatase TiO$_2$ nanoparticles with an average diameter of 15 nm [4,7], with film thicknesses in the range 3–6 μm [4,5] after drying and heat treatment. The films predominantly consist of the anatase polymorph of TiO$_2$ ($\approx$90%, with rutile making up the rest) [5,6]. The atomistic structure of the nanostructured films is not fully understood. A complete characterization of the films would involve specifying areas of the various facets exposed as well as the composition and atomic structure of each facet. To achieve this experimentally, *in situ* atomic resolution of all facets exposed in the nanostructure would be required, which is not achievable using standard surface-sensitive techniques. Computationally, the complexity of such

films means that large numbers of atoms have to be considered, rendering calculations very expensive. Instead, flat pristine surfaces are studied as model systems of the more complex nanostructures. In this way, atomic level processes can be studied on well-characterized surfaces that are likely to be those exposed in the nanostructured films. Although the large optical band gap of TiO$_2$ ($\approx$3 eV) – measured from the absorption spectrum [3] – indicates that it is unlikely to be the long-term solution as the light absorber in photoelectrochemical water splitting, the detailed characterization of atomistic and electronic structure of such model systems (bulk and pristine surfaces) available in the literature makes it a useful reference material [3,8,9]. Understanding the process of solar water splitting on a model reference material (in this case TiO$_2$) will lead to insights about the water-splitting mechanism on a generic semiconductor.

Density functional theory (DFT) calculations have predicted that the (101) surface is the most stable anatase surface [10] and represents a significant portion of the exposed surface area in macrocrystals and nanostructures [11,12]. The orientation of the facets observed on anatase macrocrystals are consistent with the computed surface energies [8]. The (101) surface cleaved from single crystals has been studied extensively with various experimental methods, including low-energy electron diffraction (LEED), scanning tunneling microscopy (STM), and x-ray photoelectron spectroscopy (XPS). STM images of this surface show large flat terraces with one bright spot per lattice unit surrounded by steps to other large terraces. The terraces are flat (101) facets and under typical conditions (tunneling into the surface at +1.5 V bias and 1.23 nA tunneling current [9]) the bright spots observed are elongated (oval). Analysis of the relative positions of the bright spots on a surface with/without adsorbates – using adsorbates expected to adsorb at Ti sites – suggests that they are likely to be situated above the bond between the undercoordinated Ti and O atoms [8,9]. These observations were confirmed by DFT calculations using the generalized gradient approximation

*ffs05@imperial.ac.uk

(GGA) [11,13,14]. Constant height STM images simulated within the Tersoff-Haman approximation show oval "bright spots" stretching over the undercoordinated Ti and O ions [13,14], in agreement with the observed STM images. The energetics and structure of the step edges between the terraces have been analyzed using DFT-GGA calculations [13]. By analyzing the types of steps formed on various vicinal surfaces, including the (516) and (514) surfaces, a number of possible step structures were proposed [13]. Several of these structures were found to have similar energies and thus would be expected to be present on an equilibrated surface, including the (516) surface. The proposed step structures are characterized by five- and four-coordinate Ti ions and two-coordinate O ions [13]. In order to improve the understanding of the structure of the step edges, Li *et. al.* studied a surface vicinal to the (101) surface with STM and LEED [15]. In this work, the vicinal surface was created by miscutting a single crystal by $10°$ relative to the (101) plane. It was suggested that the miscut surface is in either the (514) or the (516) plane. The expectation was that STM images of the vicinal surface would resemble those of the (101) surface (flat terraces separated by steps) but with a higher concentration of steps. However, both the LEED diffraction patterns and STM images suggest that, in fact, a vicinal surface structure forms. Two microfaceted models of the surface with two distinct ridges were proposed, but the STM and LEED data were insufficient to determine conclusively which of the proposed models was in better agreement with the microscopy and diffraction data. Thus, the atomic structure of the surface exposed by the miscut remains unresolved.

In addition to the (101) surface, other anatase surfaces have been found to be relatively stable, in particular the surface formation energy of the (001) surface has been calculated to be low and has been observed in nanostructured systems [11,16]. The clean (001) surface has been studied using LEED, STM, XPS, and reflection high-energy electron diffraction (RHEED), as well as DFT calculations, in particular using the local density approximation and GGA [17–19]. The computed formation energies suggest that the (001) surface is most stable in a (4×1) reconstruction [18]. This reconstruction has also been observed using LEED and XPS [17,19]. Equilibrium morphologies predicted by the Wulff constructions based on surface energies – obtained from DFT-GGA calculations – of the anatase macrocrystal show that both the (101) and the (001) surfaces are exposed [11]. Anatase particles of ≈ 1 μm diameter have been reported to have a similar structure as the computed morphology, also exposing the (101) and (001) surfaces [16]. During the study of photocatalytic oxidation of Pb^{2+} to PbO_2 on these anatase particles in solution a larger amount of PbO_2 was observed on the (001) facets than on the (101) facets [16]. This observation is attributed to a higher reactivity for photocatalytic reactions of the (001) surface relative to the (101) surface [16]. Therefore, it is likely that this surface will play a role in the interaction between water and TiO_2 nanoparticles.

The purpose of the current study is to gain an insight into which surfaces of TiO_2 are exposed in a nanoparticle/nanostructured surface. This was achieved by studying the low-index and vicinal (516) and (514) surfaces and calculating the structure, energetics, and electronic properties. For comparison to observed STM images, constant-current STM images are simulated. Here we use the hybrid exchange B3LYP functional (where a proportion of Fock exchange is included in the electronic exchange potential), as it has been previously documented that the use of this functional gives an accurate description of the structural energetics and of the electronic structure for periodic transition metal oxides [20–31]. The implementation of hybrid exchange functionals using local atomic basis sets, as in the CRYSTAL code, is computationally efficient for large periodic systems [32,33]. Furthermore, local basis sets facilitate a local chemical analysis of the electronic structure. Typically, for the TiO_2 surfaces studied in this work, STM images are obtained by tunneling electrons into the surface; therefore, simulating these STM images requires an accurate description of the states at the bottom of the conduction band. It has previously been shown that using an atom-centered Gaussian basis set optimized with respect to the ground-state energy does not describe the long-range tails of the valence and conduction bands in the vacuum above the surface sufficiently accurately [34]. This issue has been addressed by Di Valentin by adding non atom-centered functions above the surface [34]. More recently, an alternative approach has been shown to produce similar results [35]. This approach involves enhancing the basis sets of surface atoms and has the advantage of not requiring *ad hoc* decisions on the position of additional functions. This is especially important for complex surface geometries, such as the (516) and (514) surfaces.

This paper is organized as follows. In Sec. II the computational details are provided. Section III contains the results and discussion. Initially, the bulk structure of anatase is described for reference, followed by the surface structures of the (101), (001), (100) and the two vicinal surfaces. The data from the geometry relaxations is then used to create a Wulff construction of the anatase macrocrystal. The final part of Sec. III details various electronic properties of the (101), (514), and (516) surfaces, ending in the comparison of calculated constant-current STM images of the vicinal surfaces with the literature. Conclusions are drawn in Sec. IV.

II. COMPUTATIONAL DETAILS

All calculations have been performed using the CRYSTAL09 software package [32,36], based on the expansion of the crystalline orbitals as a linear combination of a local basis set (BS) consisting of atom-centered Gaussian orbitals. The titanium and oxygen ions are described by a triple valence all-electron BS: an 86-411(d31) contraction (one s, four sp, and two d shells) and an 8-411(d1) contraction (one s, three sp, and one d shells), respectively [21]; the most diffuse sp (d) exponents are $\alpha^{Ti} = 0.3297$ (0.26) and $\alpha^{O} = 0.1843$ (0.6) $bohr^{-2}$. These BSs were developed in previous studies of the bulk and surface phases of titania, in which a systematic hierarchy of all-electron BSs was used to quantify the effects of using a finite BS [37,38].

Electronic exchange and correlation are approximated using the hybrid exchange B3LYP functional. Matrix elements of the exchange and correlation potentials and the energy functional are integrated numerically on an atom-centered grid of points. The integration over radial and angular coordinates is performed using Gauss-Legendre and Lebedev schemes,

respectively. A pruned grid consisting of 75 radial points and 5 subintervals with (50, 146, 194, 434, 194) angular points has been used for all calculations (the XXLGRID option implemented in CRYSTAL09 [32]). This grid converges the integrated charge density to an accuracy of about $\times 10^{-6}$ electrons per formula unit. The Coulomb and exchange series are summed directly and truncated using an overlap criterion with thresholds of 10^{-7}, 10^{-7}, 10^{-7}, 10^{-7}, and 10^{-14}, as described previously [32,39]. Reciprocal space sampling for the bulk structure was performed on a Pack-Monkhorst net with a shrinking factor IS = 8 along each periodic direction.

Structural optimization was performed using the Broyden-Fletcher-Goldfarb-Shanno scheme, as implemented in CRYSTAL09 [32]. Convergence was determined from the root mean square (rms) and the absolute value of the largest component of the forces. The thresholds for the maximum and the rms forces (the maximum and the rms atomic displacements) have been set to 0.00045 and 0.00030 (0.00180 and 0.0012) in atomic units. Geometry optimization was terminated when all four conditions were satisfied simultaneously. Projection of the density of states was performed using Mulliken analysis.

For the simulation of constant-current STM images diffuse orbitals were added to the BSs of all undercoordinated Ti and O atoms on both vicinal surfaces. For the Ti (O) ions an extra d (p) orbital was added with $\alpha = 0.06$ bohr^{-2}. The resulting (enhanced) BSs are described in detail in Ref. [35]. This methodology has been shown to reproduce accurately STM images for low-index surfaces of anatase and rutile TiO$_2$ [35]. To reflect the positive bias used experimentally [15], the states sampled in this study were those within 0.76 eV of the conduction band minimum. The value of 0.76 eV reflects the $+0.76$ V bias applied for the highest-resolution STM images in Ref. [15].

III. RESULTS

The bulk geometry of anatase TiO$_2$ is presented as a reference for comparison with the surfaces studied. The low-index surfaces – (101), (100), and (001) – and the (514) and (516) surfaces are analyzed in this section in terms of atomic structure, surface formation energy, Wulff construction, and electronic structure. Finally, the simulated constant-current STM images for the vicinal surfaces are presented.

A. Bulk geometry

The anatase structure belongs to the $I4/amd$ tetragonal space group and the unit cell is defined by the lengths of lattice vectors $\mathbf{a_B}$ and $\mathbf{c_B}$ (the subscript $\mathbf{B}$ denoting the bulk phase) and the oxygen internal coordinate u. The primitive cell contains two atoms in the asymmetric unit: a Ti ion at $(0,0,0)$ and an O ion at $(0,0,u)$, in fractional coordinates. The predicted structural parameters, with the deviation from those deduced from pulsed neutron diffraction at 15 K [40] in parentheses, are length of $\mathbf{a_B} = 3.794$ Å (0.32%), length of $\mathbf{c_B} = 9.768$ Å (2.80%), $u = 0.205$ (1.44%), and $V_{\mathbf{B}} = 70.31$ Å^3 (2.87%). These parameters are also in close agreement with previous calculations using the B3LYP functional [41]. Each Ti is octahedrally coordinated to six O ions. The TiO$_6$ octahedron is distorted, with the length of the two apical

TABLE I. Details of all the surfaces considered here. In the column "Sequence," the stacking sequence of the atomic layers in the nonperiodic direction (z) is indicated for the repeat unit of the unrelaxed slab, where hyphens separate atomic layers. The surface unit-cell vectors (in Å) and area (Å^2) along with the angle γ ($^\circ$) are also tabulated.

Miller indices	Sequence	Area	**a**	**b**	γ
(1 0 0)	2Ti 4O	37.064	3.794	9.768	90.00
(0 0 1)	O-Ti-O	14.396	3.794	3.794	90.00
(1 0 1)	O-Ti-O-O-Ti-O	19.881	3.794	5.572	109.90
(5 1 4)	O-Ti-O-O-Ti-O	98.783	5.572	17.859	97.00
(5 1 6)	2O-2Ti-2O	103.896	5.572	18.649	91.25

Ti-O$_{ap}$ bonds slightly longer than the four equatorial, Ti-O$_{eq}$, bonds. The calculated (observed) lengths (in Å) being 2.000 (1.980) for Ti-O$_{ap}$ and 1.948 (1.935) for Ti-O$_{eq}$ [40]. The anatase TiO$_6$ octahedron shares four edges in adjacent pairs. This is in contrast with that in the rutile structure, where the octahedron shares only two opposite edges [40]; the resulting structure is characterized by zigzagging octahedra along the $\mathbf{a_B}$ and $\mathbf{c_B}$ lattice vectors [41].

B. Surface structure

The atomistic structure of the (101), (100), and (001) surfaces has been studied previously using DFT calculations using all electron local atomic BSs as well as the plane-wave-pseudopotential approximation [10,11,18]. Lattice parameters for these surfaces derived from the optimized bulk structure are listed in Table I along with those of the two vicinal surfaces. The surface terminations were chosen so that the slabs are stoichiometric and nonpolar in the nonperiodic direction. In terms of the Tasker surface classification, the surfaces studied here are all Type 2, with the exception of the (100) surface, which is Type 1 [42]. The sequence of the atomic layers that make up these slabs are provided in Table I.

The (101) surface has two possible terminations, both resulting in stoichiometric, nonpolar (Tasker type 2) surfaces [10]. One of them has a significantly higher calculated surface formation energy (1.27 J m^{-2}), which is likely to be due to lower coordination of the surface ions: one Ti$_{4c}$ ion as well as two O$_{2c}$ ions are exposed at the surface per unit cell; the subscript nc indicates that the ion is n-fold coordinated. In this study we have only considered the low-energy termination ($E_s = 0.56$ J m^{-2}), where, as shown in Fig. 1, one of each of the following are exposed: O$_{2c}$, O$_{3c}$, Ti$_{5c}$, and Ti$_{6c}$. The O$_{2c}$ bridges a Ti$_{5c}$ and a Ti$_{6c}$ ion, producing the characteristic saw-tooth (101) surface structure. The computed displacements with respect to the unrelaxed geometry cut from the optimized bulk are listed in Table II and are in good agreement with those from previous DFT calculations both with and without the use of hybrid exchange functionals [10,11]. The undercoordinated Ti relaxes inwards, while the undercoordinated O relaxes outwards.

The (100) surface consists of terraces separated by grooves. On the terraces, two Ti$_{5c}$ are exposed, as well as two O$_{2c}$ and two O$_{3c}$. In the grooves two Ti$_{6c}$ ions are present along with two O$_{3c}$ per unit cell. Each atomic layer consists of a Ti$_2$O$_4$

(514) surface

(516) surface

Planar Unrelaxed Termination

Planar Unrelaxed Termination

Proposed Unrelaxed Termination

Proposed Unrelaxed Termination

Proposed Relaxed Termination

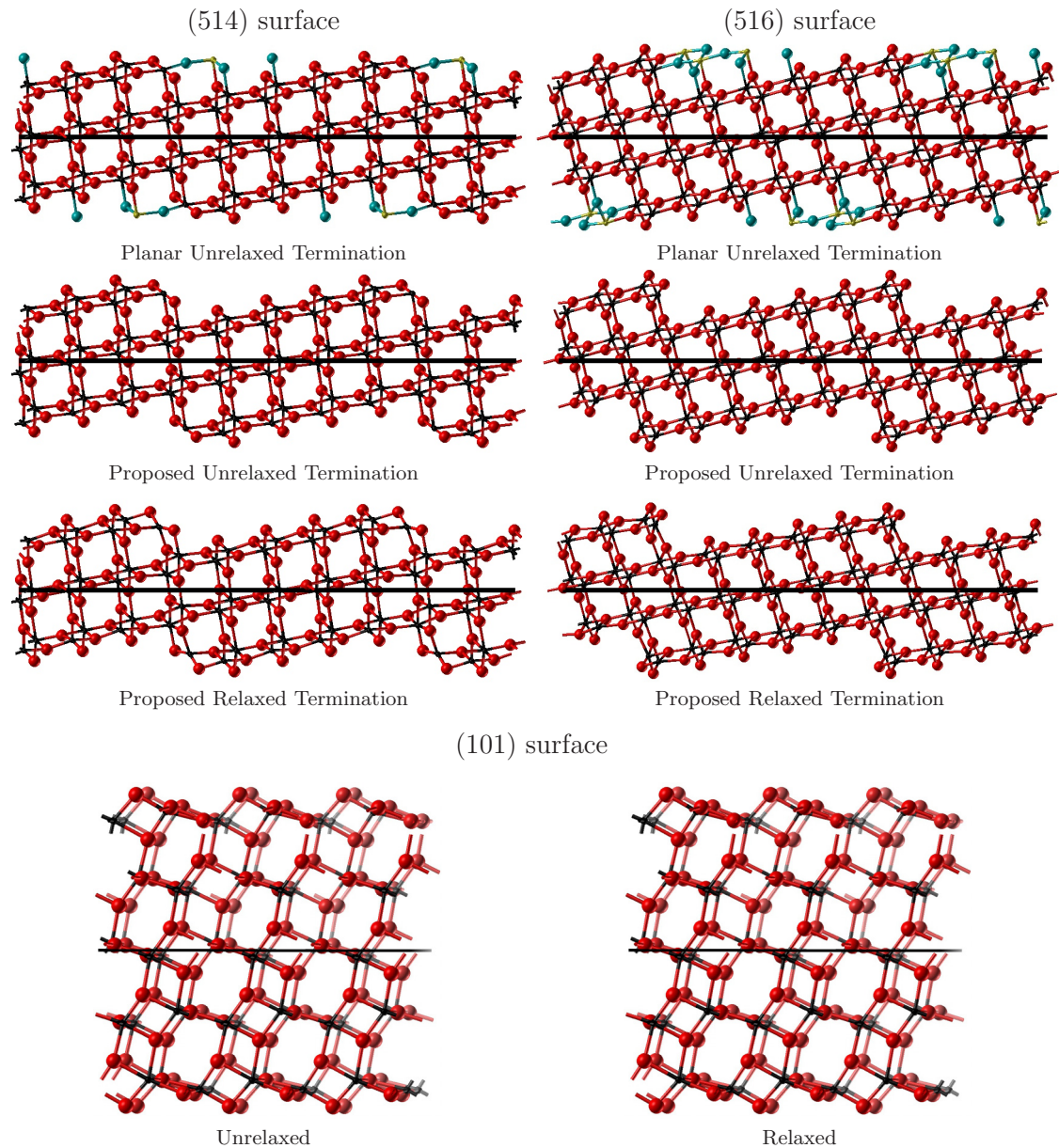Proposed Relaxed Termination

(101) surface

Unrelaxed

Relaxed

FIG. 1. (Color online) 3D representations of the (514), (516), and (101) anatase surfaces. Small (black) spheres represent Ti atoms and large (red) spheres represent O atoms. The atoms highlighted in the pictures at the top need to be removed in order to define the reconstructed surface. To facilitate the visualization of the terraces in the (514) and (516) surfaces, the images shown here represent a (1×2) periodicity. The (101) surface depicted in the 2×3 periodicity.

unit. As with the (101) surface, good agreement was observed between the computed relaxation displacements of the (100) surface and those in previous work [10].

The (001) surface is relatively flat and, besides one Ti_{5c}, it exposes one O_{2c} and one O_{3c} per unit cell. The O_{2c} bridges two Ti_{5c} ions (the two Ti ions are related by translational symmetry). Retaining the high symmetry of the surface as cleaved from the bulk means the surface remains in a bulklike geometry and has a very high E_s (1.23 J m^{-2}), whereas removal of these constraints allows the system to relax to a more stable geometry (E_s of 1.03 J m^{-2}), which is comparable to that reported from previous calculations [11].

When considering the planar unrelaxed terminations of the (514) and (516) surfaces (depicted in Fig. 1), it is

clear that the outermost atoms have a lower coordination than those on the (101) surface: the monocoordinate O ions and the three-coordinate Ti ions are highlighted in Fig. 1. The removal of these strongly undercoordinated ions results in the presence of more highly undercoordinated atoms, also highlighted. From this an algorithm was developed to remove ions coordinated to a chemically unrealistic number of counterions (e.g., monocoordinate O, or three-coordinate Ti ions), while maintaining stoichiometry and nonpolarity in the nonperiodic direction. This approach is different from other methods for determining the composition of a surface termination more commonly used, where atoms are added to increase the coordination of the outermost atoms [18]. The approach used here has the advantage that no *ad hoc* decisions

TABLE II. Displacements (in Å) of the 12 outermost atoms during the relaxation of the relaxed (101) surface with respect to the unrelaxed geometry cut from the optimized bulk. Labeling is based on Fig. 4 in Ref. [10]. There is no displacement along $[0\bar{1}0]$ due to symmetry constraints. The [101] direction is perpendicular to the (101) plane and, in this case, is equivalent to the z axis.

	This work		From Ref. [10]	
Label	$[10\bar{1}]$	[101]	$[10\bar{1}]$	[101]
O_1	0.36	-0.01	0.37	-0.01
Ti_2	0.10	-0.18	0.11	-0.17
O_3	0.23	0.21	0.25	0.21
O_4	0.23	0.07	0.25	0.06
Ti_5	0.24	0.21	0.26	0.20
O_6	0.23	-0.06	0.24	-0.06
O_7	0.13	0.03	0.15	0.03
Ti_8	0.04	-0.12	0.04	-0.11
O_9	0.08	-0.02	0.08	-0.04
O_{10}	0.10	0.02	0.11	0.03
Ti_{11}	0.11	0.11	0.11	0.09
O_{12}	0.06	-0.02	0.06	-0.03

regarding the coordinates of added atoms have to be made. The surface structure of the (514) and (516) surfaces (obtained by using this algorithm) consist of long terraces interrupted by step edges. The terraces expose four O_{2c}-Ti_{5c} pairs on both the (514) and the (516) surfaces. The bond angles and bond lengths presented in Table III illustrate the similarity between the terraces of both vicinal surfaces and the (101) surface. The short Ti-O bond between the Ti_{5c} and a O_{3c} in the subsurface layer (1.778 Å) is due to the inward relaxation of the Ti, analogous to the computed relaxation of the (101) surface. It should be noted that, due to the shape of the step in the vicinal surfaces, an "inward" relaxation does not necessarily translate into a displacement along the nonperiodic z direction [as is the case for the (101) surface]. The steps display different coordination and geometry to the terraces. The (516) surface step consists of two Ti_{5c} and two O_{2c} per surface unit cell, with each O_{2c} bridging the two Ti_{5c}. The (514) surface step consists of one Ti_{4c} and two O_{2c} per surface unit cell. One O_{2c} bridges a Ti_{5c} and the Ti_{4c}, while the other O_{2c} bridges a Ti_{6c}

TABLE III. Bond lengths and bond angles between various surface atoms in the (101), (514), and (516) surfaces. The subscript adjacent to Ti an O indicates the coordination of the atoms in question. In the case of the vicinal surfaces a range of values are given, representing different O_{2c}-Ti_{5c} pairs on the terraces.

	Bond length (Å)			
Atoms Involved	(101)	(516) Terrace	(514) Terrace	(516) Step
O_{2c}-Ti_{5c}	1.834	1.829–1.833	1.831–1.835	1.813–1.815
O_{2c}-Ti_{5c}				1.879–1.889
O_{3c}-Ti_{5c}	1.778	1.778–1.781	1.776–1.785	1.776–1.779
O_{3c}-Ti_{5c}	2.057	2.065–2.074	2.077–2.090	2.022–2.044
O_{3c}-Ti_{5c}	1.988	1.964–1.973	1.967–1.977	2.231–2.239
O_{3c}-Ti_{5c}	1.988	1.953–1.999	1.950–1.966	
O_{2c}-Ti_{6c}	1.841	1.953–1.999	1.835–1.846	
	Angle (degrees)			
Ti_{6c}-O_{2c}-Ti_{5c}	102.3	101.3–101.9	101.7–102.1	

and the Ti_{4c}. This is in good agreement with the step structures outlined in Ref. [13]. The Ti_{5c}-Ti_{5c} distance at the (516) step (2.930 Å) is shorter than that of the (101) surface (3.794 Å) and is, in fact, comparable to the Ti_{5c}-Ti_{5c} separation at the rutile (110) surface. The two Ti_{5c} along with the O_{2c} bridging the two Ti_{5c} ions at the (516) surface step and the Ti_{4c} on the (514) surface are possible active adsorption sites in the photocatalysis of water.

C. Surface formation energy and Wulff construction

The relative stability of the surfaces considered has been assessed by evaluating the surface formation energy per unit area, E_s, which, for a stoichiometric slab, is defined as

$$E_s = \frac{1}{2A}\left(E_{\text{slab}} - nE_{\text{bulk}}\right), \qquad (1)$$

where E_{slab} is the total energy of the slab, E_{bulk} is the total energy per formula unit in the bulk, n is the number of formula units per unit cell of the slab, and A is the unit-cell area. The surface formation energy of the two vicinal surfaces and of the low-index surfaces, i.e. (100), (001), and (101), is plotted as a function of the slab thickness in Fig. 2. The (100) surface
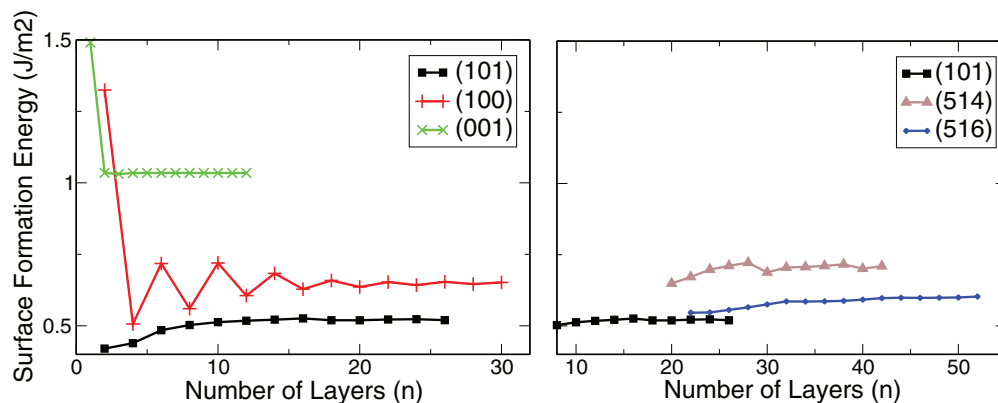

FIG. 2. (Color online) Surface formation energy as a function of the slab thickness, expressed in terms of the number of formula units in the slab.

TABLE IV. Surface formation energies (E_s), converged to ± 0.005 J/m^2, corresponding thickness and number of layers (equivalent to the number of formula units) for various anatase TiO$_2$ surfaces. The (001)r represents the (4 × 1) reconstruction of the (001) surface.

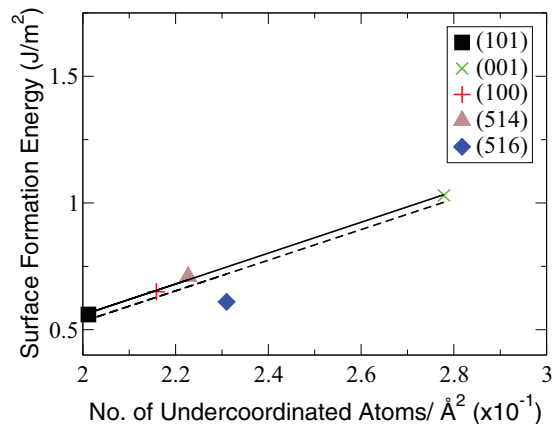| Miller indices	E_s (J/m^2)	No. of layers	Thickness (Å)
(101)	0.56	10	16.48
(100)	0.65	20	12.80
(001)r	0.62	10	23.55
(001)	1.03	4	10.68
(514)	0.71	32	12.19
(516)	0.61	30	12.29

FIG. 3. (Color online) Surface formation energy of various anatase surfaces as a function of under coordinated atoms per unit area. The dotted line is a linear fit of all the points. The solid line is a linear fit of the three low-index surfaces.

shows strong oscillation; this has been reported before [10] and is reminiscent of the behavior of the rutile (110) surface [43].

From the values of E_s in Table IV, it is clear that the (101) surface is the most stable with a computed E_s of 0.56 J/m^2, in agreement with previous studies [8,10]. The computed E_s of both vicinal surfaces is relatively low; this is especially true for the (516) surface, where E_s is comparable to that of the (101) surface. This is in good agreement with previous calculations [13]. Both vicinal surfaces have a lower calculated E_s than the (001) surface, which has been shown to be present in small particles (≈ 1 μm diameter) [16], as well as in Wulff constructions based on DFT calculations [11,18]. The values of E_s reported in Table IV are for both the unreconstructed surface and the more stable (4 × 1) reconstruction studied previously [11,17,19]. For better comparison, the most stable structure of the (4 × 1) reconstruction described in Ref. [11] was used as a starting point for the geometry relaxation. The resulting surface formation energy is 0.62 J/m^2. This value is lower than the E_s of the (514) surface and is effectively identical to the E_s of the (516) surface

In order to rationalize the different surface formation energies, we have plotted E_s as a function of the number of undercoordinated atoms per unit area (see Fig. 3). There is a clear linear trend: the higher the number of under-coordinated atoms, the higher is the surface formation energy. The exception is the (516) surface; given the number of undercoordinated atoms per unit area, we would expect the surface to have a higher E_s. A possible explanation for the higher relative stability of the (516) surface is that the Ti$_{5c}$-O$_{2c}$-Ti$_{5c}$ motif stabilizes the O$_{2c}$ ion. The (001) surface is the only other anatase surface studied to exhibit an O$_{2c}$ coordinated to two Ti$_{5c}$ ions; however, in the (1 × 1) periodicity the Ti$_{5c}$-O$_{2c}$-Ti$_{5c}$ exhibits lopsided bond lengths around the O$_{2c}$ (computed to be 1.725 Å and 2.271 Å). These "unnatural" bond lengths at the (001) surface have been cited as the driving force behind the computed and observed (4 × 1) reconstruction [17–19], in which the O$_{2c}$ ions are less constrained and can relax to a more stable geometry. The imposition of the (1 × 1) periodicity on the (001) surface restricts the relaxation of the Ti$_{5c}$-O$_{2c}$-Ti$_{5c}$ motif, resulting in a higher relative E_s. Conversely, the less constrained relaxation of the Ti$_{5c}$-O$_{2c}$-Ti$_{5c}$ motif at the (516) surface results in bond lengths of 1.815 and 1.889 Å. These values are similar to those computed for the Ti$_{6c}$-O$_{2c}$-Ti$_{5c}$ motif at the (101) surface (see Table III) as well as the bond lengths for the Ti$_{5c}$-O$_{2c}$-Ti$_{5c}$ motif at the (4 × 1) reconstruction

of the (001) surface calculated previously [18]. Therefore, we propose that the presence of the Ti$_{5c}$-O$_{2c}$-Ti$_{5c}$ motif in a stable geometry at the (516) surface step leads to a stabilization of the O$_{2c}$ ion and, thus, results in the lowering of the E_s with respect to the other surfaces studied. A similar effect should be observed for the (514) surface, where an O$_{2c}$ ion bridges a Ti$_{4c}$ and a Ti$_{5c}$. In this instance it appears that the stabilization of the O$_{2c}$ is offset by the exposure of a Ti$_{4c}$ ion.

The equilibrium morphology of an anatase macrocrystal, as predicted by the Wulff construction, using the surface formation energies of all the surfaces studied in the current work is presented in Fig. 4. For comparison, a Wulff construction based only on the low-index surfaces is also included, where the (101) surface is dominant (accounting for 96% of the total surface area) with the (001) surface making up the rest; the (100) surface is not exposed at all, in agreement
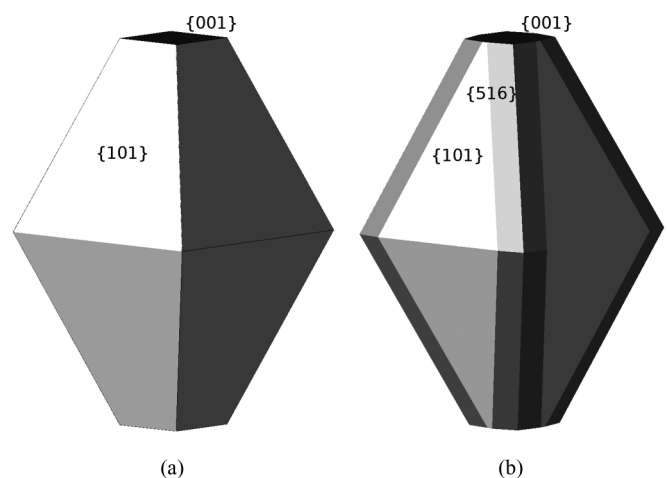

FIG. 4. Wulff constructions of anatase TiO$_2$. In both cases the unreconstructed (001) surface formation energy was used. Using the surface formation energy of the more stable reconstruction leads to a tighter truncation in the [001] direction and, thus, a larger (001) surface area. (a) Low-index surfaces only; (b) low-index and vicinal surfaces.

with previous work [11,12,44]. When both vicinal surfaces are considered, the (516) surface is exposed along with the (101) and (001) surfaces. The (101) surface is still dominant (70%); nevertheless, the (516) accounts for approximately 27% of

the total surface area. The (516) surface is exposed at the boundary between the different symmetry equivalent facets of the (101) surface. We have not included the Wulff construction using more stable (4×1) reconstruction of the (001) surface
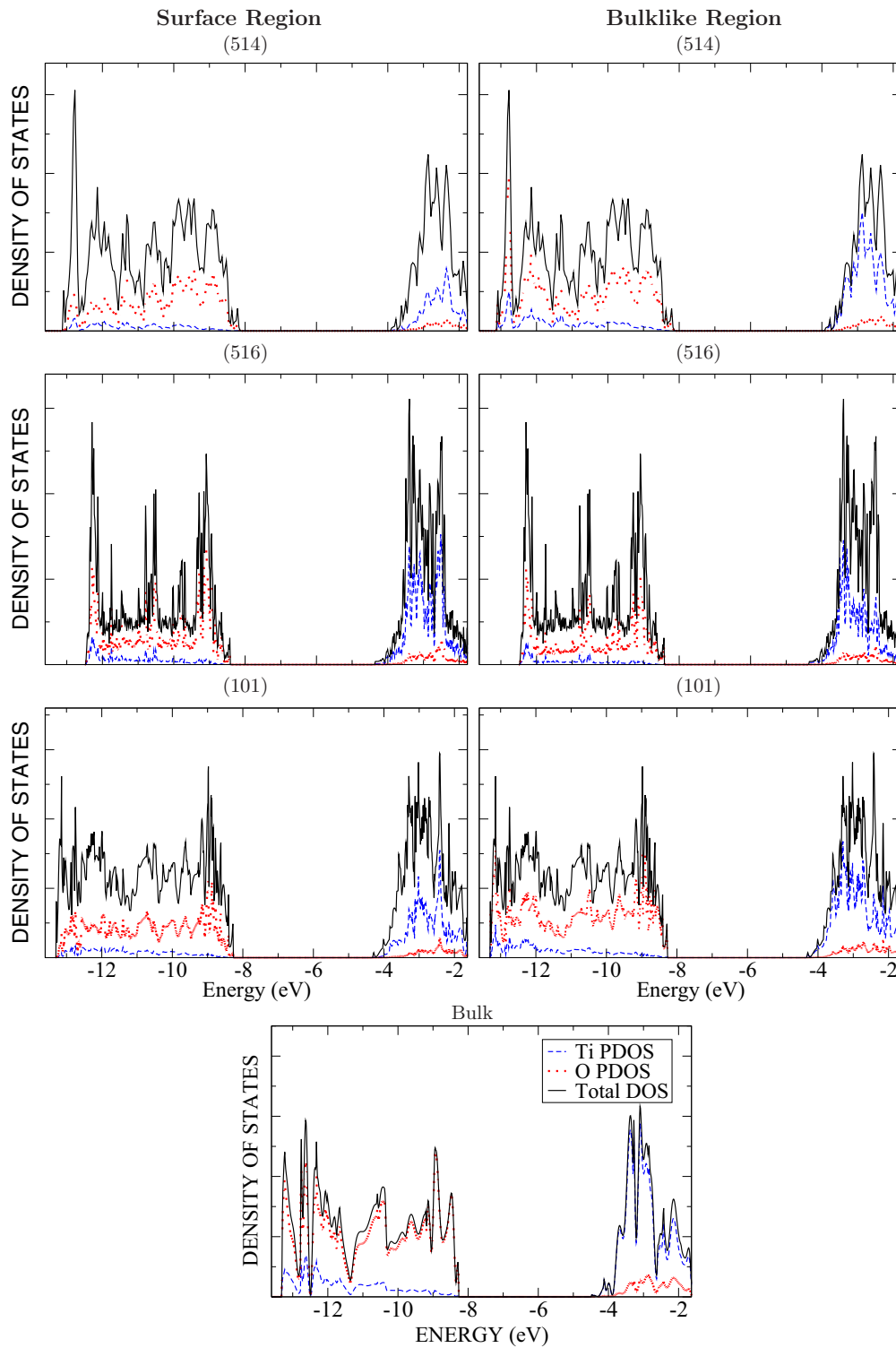

FIG. 5. (Color online) Projected density of states for the (514), (516), and (101) surfaces and bulk anatase. Solid (black) lines represent total DOS, dashed (blue) lines represent the DOS projected over Ti ions and dotted (red) lines represent the DOS projected over O ions. In the plots on the left (labeled "Surface region") the DOS is projected over Ti and O ions exposed at the surface, while in the plots on the right (labeled "Bulklike region") the DOS is projected over the remaining ions in the slab. The DOS of bulk anatase is shown at the bottom with the DOS projected over all Ti and O ions. The top of the bulk VB has been aligned to the top of the (101) surface VB for comparison.

TABLE V. Valence band (VB) maxima and conduction band (CB) minima for the surfaces considered here in eV.

Miller indices	VB maximum (eV)	CB minimum (eV)
(101)	−8.24	−4.45
(100)	−7.85	−4.05
(001)[a]	−7.33	−3.78
(516)	−8.35	−4.51
(514)	−8.05	−4.19

[a]The band edges for the (001) are for the unreconstructed surface.

in Fig. 4. However, using the calculated E_s of 0.62 J/m^2 an alternative Wulff construction was obtained for the case including the vicinal surfaces. It is identical in shape, with the exception that the (001) facets account for a higher ratio of the exposed surface (17%). The (516) surface is still exposed, and the (101) surface still accounts for the majority (54%) of the total surface area. The shape of the macrocrystals predicted by Wulff constructions is similar to that of nanoparticles – simulated using a more sophisticated formalism that also takes into account edge and corner effects [12,44,45] – as well as small particles observed experimentally [16]. It is, therefore, likely that surfaces exposed in the equilibrium morphologies of anatase crystallites calculated here are also present in nanoparticles/nanostructures.
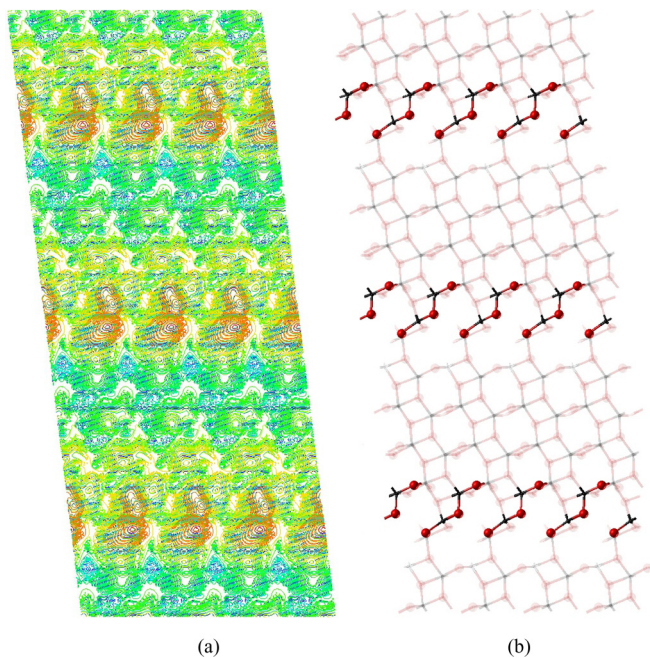
D. Electronic properties

Anatase TiO$_2$ is an indirect band-gap semiconductor with an optical band gap of approximately 3.2 eV (measured from the absorption spectrum) [3]. The single-particle band gap of the bulk was calculated to be 3.77 eV. This value is the fundamental band gap and is in good agreement with previous calculations [41,46]. As expected for the anatase TiO$_2$ polymorph, all surfaces have an indirect band gap and most of the surfaces display no surface states in the band gap. The exception is the (001) surface; however, the surface states are only present in the bulklike, symmetry-constrained surface structure and are, thus, attributed to the instability of that system.

The total and projected density of states (PDOS) of the (516), (514), and (101) surfaces are shown in Fig. 5 along with that of the bulk crystal for comparison. In the PDOS of bulk anatase the valence band (VB) – below −8 eV – displays predominantly O-2p character, with some hybridization with Ti-3d orbitals. The conduction band (CB) – above −5 eV – is derived mainly from Ti-3d atomic orbitals with some hybridization with O-2p orbitals. These characteristics are also observed for all the surfaces presented in Fig. 5. Clearly, the PDOS of the surfaces studied here are very similar in
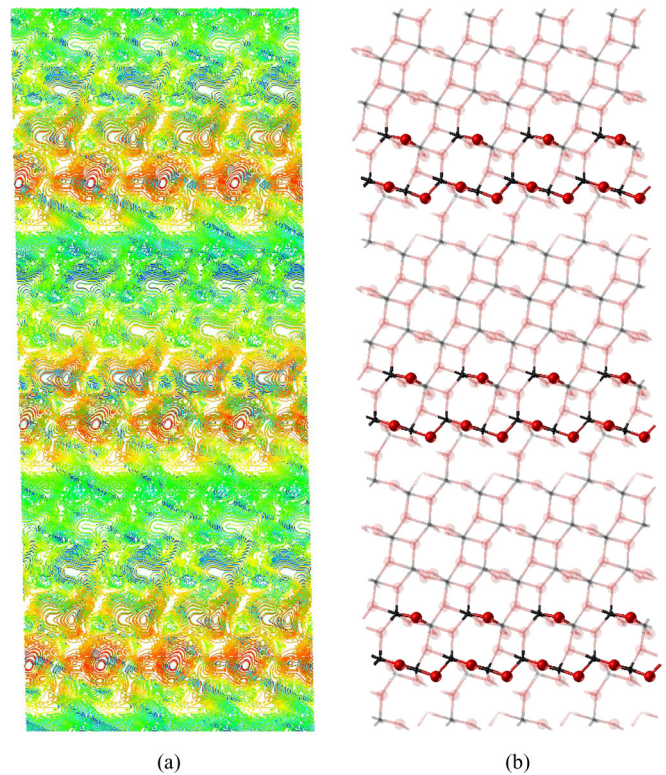
(a)   (b)

FIG. 6. (Color online) (a) Constant-current STM image of 4×3 supercell of the (514) surface (bias potential 0.75 V, 5×10^{-6} e/bohr^3). Contours are of the height of the STM tip above the surface. Red indicates a large height and, thus, a bright spot. Blue/green colors are indicative of lower values of height and, thus, represent darker areas of an STM images. (b) Top view of a 4×3 supercell of the (514) surface. Atoms highlighted are the Ti$_{4c}$ at the step; the two O$_{2c}$ coordinated to the Ti$_{4c}$ and the O$_{2c}$-Ti$_{5c}$ pair nearest to the step. These are the atoms attributed to the bright spots in (a).

(a)   (b)

FIG. 7. (Color online) (a) Constant-current STM image of 4×3 supercell of the (516) surface (bias potential 0.75 V, 5×10^{-6} e/bohr^3). Contours are of the height of the STM tip above the surface. Red indicating a large height and, thus, a bright spot. Blue/green colors are indicative of lower values of height and, thus, represent darker areas of an STM images. (b) Top view of a 4×3 supercell of the (516) surface. Atoms highlighted are the two Ti$_{5c}$ at the step, the two O$_{2c}$ coordinated to the Ti$_{5c}$ at the step, and the O$_{2c}$-Ti$_{5c}$ pair nearest to the step. These are the atoms attributed to the bright spots in (a).

terms of position and composition of the VBs/CBs. The VB (CB) maxima (minima) of all the surfaces studied are presented in Table V. As the calculations are performed with vacuum boundary conditions perpendicular to the surface the

absolute position of the band edges can be compared to that determined in, for instance, photoelectron and inverse photoelectron spectroscopy. The computed positions of the VB edges are in good agreement with those measured and
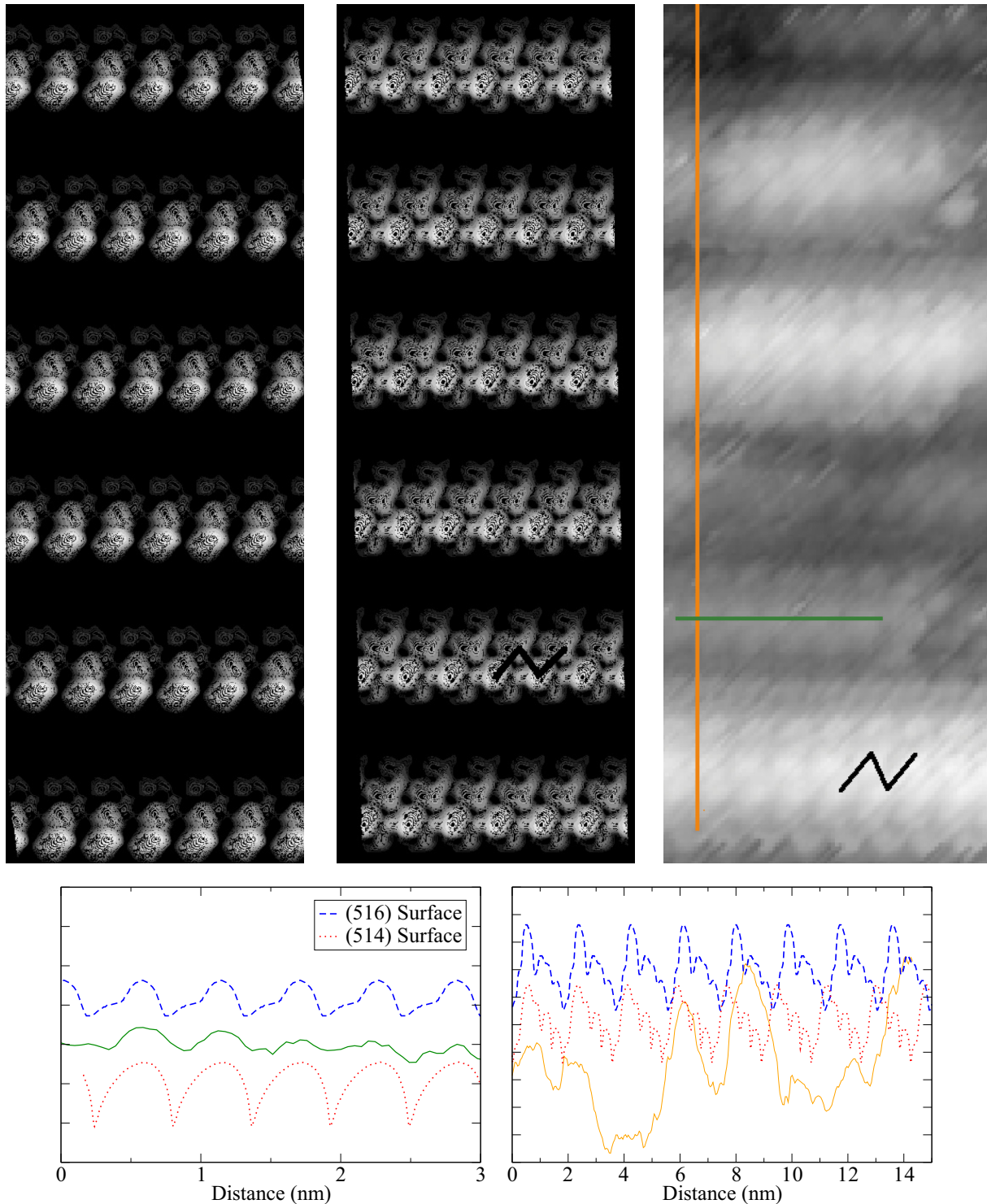

FIG. 8. (Color online) (Top row, left to right) Calculated STM image of a 6 × 6 supercell of the (514) surface (details in Fig. 6); calculated STM image of a 6 × 6 supercell of the (516) surface (details in Fig. 7); 8 × 14-nm STM image of surface first observed in Ref. [15] (+0.76 V sample bias, 0.142 nA). (Bottom row) Line profiles from the experimental and calculated STM images along the rows of bright spots (left) and perpendicular to that (right), as indicated by the horizontal (green) and vertical (orange) lines in the experimental image. Solid (green/orange) traces are from the experimental image, dashed (blue) traces are from the calculated (516) image, and dotted (red) traces are from the calculated (514) image. The distance between tick marks on the y axis corresponds to 1 Å.

calculated for a bulklike system in Ref. [47]. The CB edges are all less negative than the value reported in Ref. [47]. However, this is expected as the values computed here are of the fundamental band edges, whereas the measured optical band gap was used in the calculation of the CB edge position in Ref. [47]. The (001) surface has the highest VB edge, while the (516) surface has the lowest CB edge. Of the low-index surfaces the (101) has the lowest CB edge. Therefore, the presence of the (516) surface could have a significant effect on photocatalytic processes, e.g., in nanostructures systems.

For comparison with STM images measured in Ref. [15] constant-current STM images of the vicinal surfaces were simulated using the methodology outlined in Ref. [35] and are presented in Figs. 6 and 7. The contours represent the height of the STM tip above the surface. The larger the height (red colors), the brighter the region would appear in an STM image. For both vicinal surfaces the "bright spots" are centered between the positions of undercoordinated Ti and O ions, which is in line with previous calculations and observations made on other anatase surfaces [8,9,13,48]. The (514) and (516) surfaces have a pair of bright spots per unit cell. To illustrate the position of the bright spots with respect to the surface atoms, a 4×3-unit-cell top view of the respective surfaces is included in Figs. 6 and 7, along with the calculated STM images. In the case of the (516) surface the two bright spots are aligned diagonally, resulting in a a zigzag pattern in the STM image of multiple cells. This is similar to the STM images obtained experimentally at constant current [15]. The two bright spots are of similar size; the larger one is centered above a bond between one of the Ti_{5c} and an O_{2c} ion at the step. This bright spot has a small shoulder which is attributed to the other Ti_{5c} at the step. The reason for the small contribution of this Ti_{5c} is that its dangling bond points approximately perpendicular to the nonperiodic (z) direction and is, thus, somewhat shielded by other ions. The other bright spot (located diagonally above the first one in Fig. 7) is centered above another O_{2c}-Ti_{5c} bond, in this case involving the Ti_{5c} on the terrace nearest to the step. The brightness trails off symmetrically on either side of the row of zigzag bright spots. The pairs of bright spots in the STM image of the (514) surface differ in size significantly (with respect to each other), are closer together, and are almost directly above each other. The larger bright spot in this case is centered over a O_{2c}-Ti_{4c} bond; however, the bright spot is elongated towards the other O_{2c} ion at the step. This is atypical of anatase surfaces; however, this unusual observation is attributed to the low coordination of the Ti ion. The smaller spot is above a O_{2c}-Ti_{5c} bond in the terrace as in the (516) surface. However, in this case the O_{2c} is one of the two O_{2c} at the step. This results in a close proximity of the two bright spots. The O_{2c} on the terrace nearest to the step adds a slight shoulder to the second bright spot. The asymmetry between the two bright spots, and the region on either side the pairs, is also markedly different from the image obtained here for the (516) surface. To facilitate comparison to the experimental STM images, larger-scale (6×6 unit cells) STM images of both vicinal surfaces are presented in black and white in Fig. 8, along with a similarly sized, previously unpublished, STM image of the surface observed in Ref. [15]. The similarity of the zigzagging rows in the experimental image and the calculated (516) STM image is evident. By

contrast, there is little similarity between the computed STM image of the (514) surface and the one measured.

For a more quantitative comparison between the computed images and the observed images, line profiles obtained from the experimental data as well as from the computed images are included in Fig. 8. From the line profile of the experimental image we obtain a periodicity of 5.4 Å along the rows of bright spots (green line in Fig. 8), in good agreement with Ref. [15]. For both of the vicinal surfaces this periodicity corresponds well with the lattice parameter **a**, 5.57 Å (Table I). The periodicity perpendicular to the rows of bright spots (orange line in Fig. 8) in the experimental image is not uniform and is between 15 and 20 Å, as reported in Ref. [15]. The periodicity perpendicular to the rows of bright spots is 18.6 and 17.9 Å for the (516) and (514) surfaces, respectively. Both are within the experimentally observed range. The nearest-neighbor distance between bright spots in the simulated STM images of the (516) surface is approximately 3.8 Å. This is in good agreement with the experimental image in Fig. 8 and with Ref. [15]. For the (514) surface this distance is approximately 2.2 Å. The difference in height between the bright spot (top of ridge) and the dark region (bottom of ridge) of the calculated STM images are 3.88 Å for both vicinal surfaces. This is within the observed range of ridge heights of 3.5–6.0 Å [15].

Qualitative and some quantitative comparison of the two simulated STM images with the experimental STM image reported here and those in the literature [15] show that the computed STM image of the (516) surface is very similar to the experimentally obtained STM image of the miscut surface [15]. This is consistent with the lower surface formation energy of the (516) surface calculated here and previously in Ref. [13]. We, therefore, propose that the observed termination and atomistic structure of the miscut vicinal surface corresponds to that of the (516) surface presented here, rather than the microfaceted models described in Ref. [15].

IV. CONCLUSIONS

In this work we have established the atomistic structure of the (514) and (516) surfaces of anatase TiO_2 with DFT calculations using the hybrid exchange functional B3LYP. We have shown that the surface formation energy of these surfaces is low and that the (516) surface has stability comparable to that of the (101) surface. This results in a significant contribution (27%) of the (516) surface to the surface area of an equilibrium crystallite. Nevertheless, the (514) surface is at least metastable and could also be exposed in nanostructures. The simulated STM image of the (516) surface is in good agreement with those first observed in Ref. [15]. Therefore, we have presented a termination and atomistic structure of the (516) surface that is low in energy and consistent with observed STM images of a vicinal surface [15] as an alternative to previous models [15].

The significant contribution of the (516) surface to crystallites suggests that it could represent a significant portion of observed TiO_2 nanoparticle/nanostructured surfaces. Undercoordinated atoms on this surface could be preferential water adsorption/reaction sites and play an important role in water oxidation. This is especially true for the Ti_{5c} ions at the step. Establishing preferential reaction sites and overall atomistic structure of surfaces likely to be involved in the photocatalytic

production of hydrogen on anatase surfaces is an essential first step towards identifying molecular-level mechanisms that govern photocatalyst performance.

[1] http://ec.europa.eu/clima/policies/brief/eu/index_en.htm, European Union, 2013.

[2] A. Fujishima and K. Honda, Nature (London) **238**, 37 (1972).

[3] M. Gratzel, Nature (London) **414**, 338 (2001).

[4] A. Cowan, J. Tang, W. Leng, J. Durrant, and D. Klug, J. Phys. Chem. C **114**, 4208 (2010).

[5] J. Tang, J. R. Durrant, and D. R. Klug, J. Am. Chem. Soc. **130**, 13885 (2008).

[6] A. M. Peiro, C. Colombo, G. Doyle, J. Nelson, A. Mills, and J. R. Durrant, J. Phys. Chem. B **110**, 23255 (2006).

[7] L. Xiao-e, A. N. Green, S. A. Haque, A. Mills, and J. R. Durrant, J. Photochem. Photobiol. A **162**, 253 (2004).

[8] U. Diebold, Appl. Phys. A **76**, 681 (2003).

[9] W. Hebenstreit, N. Ruzycki, G. S. Herman, Y. Gao, and U. Diebold, Phys. Rev. B **62**, R16334 (2000).

[10] F. Labat, P. Baranek, and C. Adamo, J. Chem. Theory Comput. **4**, 341 (2008).

[11] M. Lazzeri, A. Vittadini, and A. Selloni, Phys. Rev. B **63**, 155409 (2001).

[12] A. Barnard and L. Curtiss, Nano Lett. **5**, 1261 (2005).

[13] X. Gong, A. Selloni, M. Batzill, and U. Diebold, Nat. Mater. **5**, 665 (2006).

[14] Y. He, O. Dulub, H. Cheng, A. Selloni, and U. Diebold, Phys. Rev. Lett. **102**, 106105 (2009).

[15] S. Li, O. Dulub, and U. Diebold, J. Phys. Chem. C **112**, 16166 (2008).

[16] T. Ohno, K. Sarukawa, and M. Matsumura, New J. Chem. **26**, 1167 (2002).

[17] G. S. Herman, M. R. Sievers, and Y. Gao, Phys. Rev. Lett. **84**, 3354 (2000).

[18] M. Lazzeri and A. Selloni, Phys. Rev. Lett. **87**, 266105 (2001).

[19] Y. Liang, S. Gan, S. A. Chambers, and E. I. Altman, Phys. Rev. B **63**, 235402 (2001).

[20] D. Muñoz, N. M. Harrison, and F. Illas, Phys. Rev. B **69**, 085115 (2004).

[21] J. Muscat, A. Wander, and N. Harrison, Chem. Phys. Lett. **342**, 397 (2001).

[22] G. Mallia and N. M. Harrison, Phys. Rev. B **75**, 165201 (2007).

[23] N. C. Wilson, S. P. Russo, J. Muscat, and N. M. Harrison, Phys. Rev. B **72**, 024110 (2005).

[24] G. Mallia, R. Orlando, M. Llunell, and R. Dovesi, in *Computational Materials Science*, edited by C. Catlow and E. Kotomin, NATO Science Series III (IOS Press, Amsterdam, 2003), Vol. 187, pp. 102–121.

[25] C. Di Valentin, G. Pacchioni, and A. Selloni, Phys. Rev. Lett. **97**, 166803 (2006).

[26] F. Corà, M. Alfredsson, G. Mallia, D. Middlemiss, W. Mackrodt, R. Dovesi, and R. Orlando, in *Principles and Applications of Density Functional Theory in Inorganic Chemistry II*, edited by N. Kaltsoyannis and J. McGrady (Springer, Berlin/Heidelberg, 2004), Vol. 113, pp. 171–232.

[27] G. C. De Fusco, L. Pisani, B. Montanari, and N. M. Harrison, Phys. Rev. B **79**, 085201 (2009).

[28] L. Liborio, G. Mallia, and N. Harrison, Phys. Rev. B **79**, 245133 (2009).

[29] C. L. Bailey, L. Liborio, G. Mallia, S. Tomić, and N. M. Harrison, Phys. Rev. B **81**, 205214 (2010).

[30] L. M. Liborio, C. L. Bailey, G. Mallia, S. Tomic, and N. M. Harrison, J. Appl. Phys. **109**, 023519 (2011).

[31] E. A. Ahmad, L. Liborio, D. Kramer, G. Mallia, A. R. Kucernak, and N. M. Harrison, Phys. Rev. B **84**, 085137 (2011).

[32] R. Dovesi, V. R. Saunders, C. Roetti, R. Orlando, C. M. Zicovich-Wilson, F. Pascale, B. Civalleri, K. Doll, N. M. Harrison, I. J. Bush *et al.*, CRYSTAL09 *User's Manual* (Università di Torino, Torino, 2010).

[33] I. J. Bush, S. Tomic, B. G. Searle, G. Mallia, C. L. Bailey, B. Montanari, L. Bernasconi, J. M. Carr, and N. M. Harrison, Proc. R. Soc. London, Ser. A **467**, 2112 (2011).

[34] C. Di Valentin, J. Chem. Phys. **127**, 154705 (2007).

[35] F. F. Sanches, G. Mallia, and N. M. Harrison, MRS Online Proc. Libr. **1494**, 339 (2013).

[36] R. Dovesi, B. Civalleri, E. Orlando, C. Roetti, and V. R. Saunders, *Reviews in Computational Chemistry* (Wiley-VCH, Wiley & Sons, New York, 2005), Vol. 21.

[37] J. Muscat, N. M. Harrison, and G. Thornton, Phys. Rev. B **59**, 2320 (1999).

[38] J. Muscat, V. Swamy, and N. M. Harrison, Phys. Rev. B **65**, 224112 (2002).

[39] C. Pisani, R. Dovesi, and C. Roetti, *Hartree-Fock ab initio Treatment of Crystalline Systems*, Lecture Notes in Chemistry Vol. 48 (Springer Verlag, Heidelberg, 1988).

[40] J. Burdett, T. Hughbanks, G. Miller, J. Richardson, Jr., and J. Smith, J. Am. Chem. Soc. **109**, 3639 (1987).

[41] F. Labat, P. Baranek, C. Domain, C. Minot, and C. Adamo, J. Chem. Phys. **126**, 154703 (2007).

[42] P. W. Tasker, J. Phys. C **12**, 4977 (1979).

[43] P. D. Mitev, K. Hermansson, B. Montanari, and K. Refson, Phys. Rev. B **81**, 134303 (2010).

[44] A. Barnard, P. Zapol, and L. Curtiss, J. Chem. Theory Comput. **1**, 107 (2005).

[45] A. Barnard and P. Zapol, J. Chem. Phys. **121**, 4276 (2004).

[46] J. Scaranto, G. Mallia, S. Giorgianni, C. Zicovich-Wilson, B. Civalleri, and N. Harrison, Surf. Sci. **600**, 305 (2006).

[47] D. O. Scanlon, C. W. Dunnill, J. Buckeridge, S. A. Shevlin, A. J. Logsdail, S. M. Woodley, C. R. A. Catlow, M. J. Powell, R. G. Palgrave, I. P. Parkin, G. W. Watson, T. W. Keal, P. Sherwood, A. Walsh, and A. A. Sokol, Nat. Mater. **12**, 798 (2013).

[48] U. Diebold, J. F. Anderson, K.-O. Ng, and D. Vanderbilt, Phys. Rev. Lett. **77**, 1322 (1996).